npj | climate and atmospheric science

www.nature.com/npjclimatsci

ARTICLE OPEN

Check for updates

Accelerated soil drying linked to increasing evaporative demand in wet regions

Yamin Qing[1,4], Shuo Wang[1,4]✉, Zong-Liang Yang[2], Pierre Gentine[3], Boen Zhang[1] and Jagger Alexander[2]

The rapid decline in soil water affects water resources, plant physiology, and agricultural development. However, the changes in soil drying rate and associated climatic mechanisms behind such changes remain poorly understood. Here, we find that wet regions have witnessed a significant increasing trend in the soil drying rate during 1980−2020, with an average increase of 6.01 − 9.90% per decade, whereas there is no consistent trend in dry regions. We also identify a near-linear relationship between the annual soil drying rate and its influencing factors associated with atmospheric aridity and high temperatures. Further, enhanced evapotranspiration by atmospheric aridity and high temperatures is the dominant factor increasing the soil drying rate in wet regions. Our results highlight the accelerated soil drying in the recent four decades in wet regions, which implies an increased risk of rapidly developing droughts, posing a serious challenge for the adaptability of ecosystems and agriculture to rapid drying.

npj Climate and Atmospheric Science (2023)6:205 ; https://doi.org/10.1038/s41612-023-00531-y

INTRODUCTION

Changes in soil moisture (SM) play a key role in the exchange of water[1–3], energy[4–6], and carbon[7–10], affecting plant transpiration and photosynthesis[11–13], microbiological and biochemical activity[14–16], as well as vegetation dynamics[17–19]. SM appears to have exhibited a long-term decreasing trend over the past few decades, at least over specific regions[20,21], and such a strong tendency towards drying may contribute to widespread increases in droughts[22,23]. Further, the rate of soil drying has substantial impacts on plant physiology and acclimation: as slowly drying stress may induce better plant acclimation than rapidly imposed stress[24–26]. However, rapidly developing soil dryness may not provide sufficient time for such acclimatory responses to occur, resulting in more severe physiological responses[27]. A rapid soil drying rate will also likely make water scarcity an even greater limitation to plant productivity across an increasing amount of global land[28]. Recent studies have tried to quantify SM trends and variabilities, but the changes in soil drying rate and associated climatic mechanisms behind such changes remain elusive.

The changes in SM are associated with a range of climatic factors that can influence SM dynamics, including temperature (T), vapor pressure deficit (VPD), radiation (Rn), and precipitation (P)[29–32]. Rapid soil drying can be triggered or exacerbated by two or more extremes that occur simultaneously. A representative example is an extreme deficit of P coinciding with a heat wave, such as the fast-developing soil drying that occurred in southern Queensland in January 2018[33]. When the simultaneous occurrences of extremes are superimposed on more slowly evolving factors such as a slow-developing SM deficit, rapid soil drying may occur. On the other hand, land and atmosphere interactions play an indirect role in accelerating soil drying. A typical example is flash drought characterized by a sudden onset and rapid soil drying with severe impacts[34,35]. P reduces the input of water into the soil, leading to insufficient SM. This may cause high near-surface air T and VPD, through land−atmosphere coupling, eventually causing a further decline in SM with a rapid drying rate[36]. The interactions between these factors are complex and can vary across different spatial and temporal scales, making it challenging to quantify the relative contributions of each factor to changes in soil drying rate. However, there is still a significant gap in our understanding of the mechanisms driving the changes in soil drying rate, highlighting the need for further research improving our understanding of rapid soil drying.

We assess changes and trends in annual soil drying rates, across the globe, for 1980–2020 using three observation-based datasets (ERA5, GLEAM, and MERRA-2). Here, the soil drying rate refers to the decline rate of soil water in the development of soil dryness (SM < 30th percentile: SM below 30th percentile indicates the occurrence of dryness, as recommended by the U.S. Drought Monitor). Additionally, we investigate potential individual factors (i.e., T, VPD, Rn, and P) and combined factors (i.e., two or three factors are combined) associated with the likelihood of rapid soil drying. Specifically, the combined factors, which consider the interactions and feedback between atmospheric factors, are used to quantify the joint effects of individual factors on the soil drying rate from a perspective of causal impact. This analysis helps to improve our understanding of the mechanisms driving the changes in soil drying rate. Our findings are expected to be useful for drought management, particularly in regions that are prone to rapidly evolving droughts, and can inform the development of effective management strategies to mitigate the impacts of soil drying on ecological and socio-economic systems.

RESULTS

Long-term changes and trends in SM mean, variability, and extreme

We choose a 5-day (pentad) sampling frequency to further detect SM variations, since large SM variability is identified at the short pentad time scale (Fig. 1a). The spatial patterns of the changes in pentad-mean and pentad-to-pentad SM variability exhibit almost opposite features during 1980–2020 (Fig. 1b, d). An overall

[1]Department of Land Surveying and Geo-Informatics, Research Institute for Land and Space, The Hong Kong Polytechnic University, Hong Kong, China. [2]Department of Geological Sciences, The John A. and Katherine G. Jackson School of Geosciences, University of Texas at Austin, Austin, TX 78712, USA. [3]Department of Earth and Environmental Engineering, Columbia University, New York, NY 10027, USA. [4]These authors contributed equally: Yamin Qing, Shuo Wang. ✉email: shuo.s.wang@polyu.edu.hk

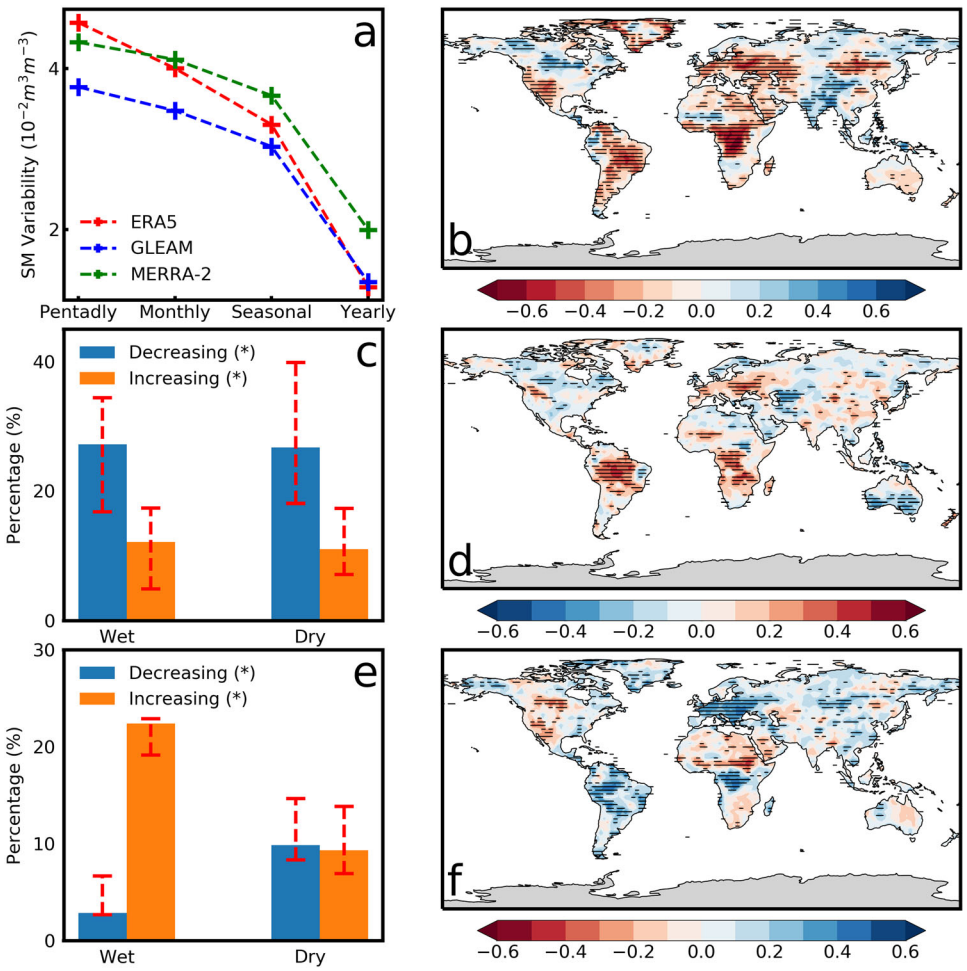

Fig. 1 SM changes in mean, variability, and extreme. a Global area–weighted average changes in SM variability on different time scales including pentad, monthly, seasonal, and yearly. **b** Spatial distribution of trend in pentad mean of SM during 1980–2020. **c** Proportion of areas showing increasing and decreasing trends in pentad mean of SM during 1980–2020 for wet and dry regions. The red dashed lines at the top of each bar represent the range of uncertainty in three different datasets. **d** Spatial distribution of trends in pentad variability of SM during 1980–2020. **e** Proportion of areas showing increasing and decreasing trends in SM decline rate during 1980–2020 for wet and dry regions. The red dashed lines at the top of each bar represent the range of uncertainty in three different datasets. **f** Spatial distribution of trends in SM decline rate during 1980–2020. * represents the regions where the trend is statistically significant at the level of 0.05. The results in **b**, **d**, **f** are obtained based on the ensemble mean of ERA5, MERRA-2, and GLEAM. Stippling represents the regions where the trend is statistically significant at the level of 0.05.

decreasing trend of pentad-mean SM is found, with 34.93−74.28% of land experiencing a significant ($p < 0.05$) drying trend. Specifically, 16.82−34.41% and 18.11−39.87% of wet and dry areas are becoming significantly drier, respectively, and the impacted areas are much wider than the areas getting wetter (4.92−17.41% and 7.14−17.34%; Fig. 1c). However, the pentad-to-pentad variability of SM shows mostly an increasing trend and parts of land areas are becoming significantly more variable, especially in Europe, south Asia, South America, and Africa, during the period of 1980−2020, suggesting in many regions SM is becoming drier and more variable. Similar trends can also be obtained for all three datasets (Supplementary Fig. 1). Further, we find that the annual SM decline rate (the difference between the current and next-pentad SM) shows an overall upward trend, especially in wet regions (Fig. 1e, f). 19.16−22.87% of wet regions show a significant increasing trend in the SM decline rate, with a global-averaged rate of 3.66 $10^{-3}m^3m^{-3}pentad^{-1}$, and 8.31−14.65% of dry regions witness a significant increasing trend in the soil decline rate (global-averaged rate of 1.81 $10^{-3}m^3m^{-3}pentad^{-1}$), indicating that the SM decline rate is accelerating, especially in wet regions (Fig. 1e). This is consistent across all three datasets (Supplementary Fig. 2).

Generally, critical damages to plants are often caused by rapid soil drying during the development of dryness conditions compared with slow drying ones, in which plants can acclimate or adapt[27]. A slow-drying rate of SM may improve the water-use efficiency of plants and increase dryness tolerance through osmotic adjustment or by altering the root–shoot allocation to lessen the resulting physiological impairment[37,38]. However, rapid soil drying provides insufficient time for plants to activate protective mechanisms under limited-water conditions, potentially causing irreversible damage to plants[27]. Therefore, the soil drying rate, which refers to the SM decline rate during the development of soil dryness (SM < 30th percentile), is examined. We find that although the annual soil drying rate varies across three reanalysis datasets, it is increasing across datasets (6.01−9.90% per decade) during the period of 1980–2020, in wet regions (Fig. 2a). On the contrary, there is no consistent trend in the mean soil drying rate in dry regions (Fig. 2b), where evaporation rate is more regulated by SM limitations[6]. Meanwhile, evapotranspiration (ET) has witnessed a significant and steady increase during the period of

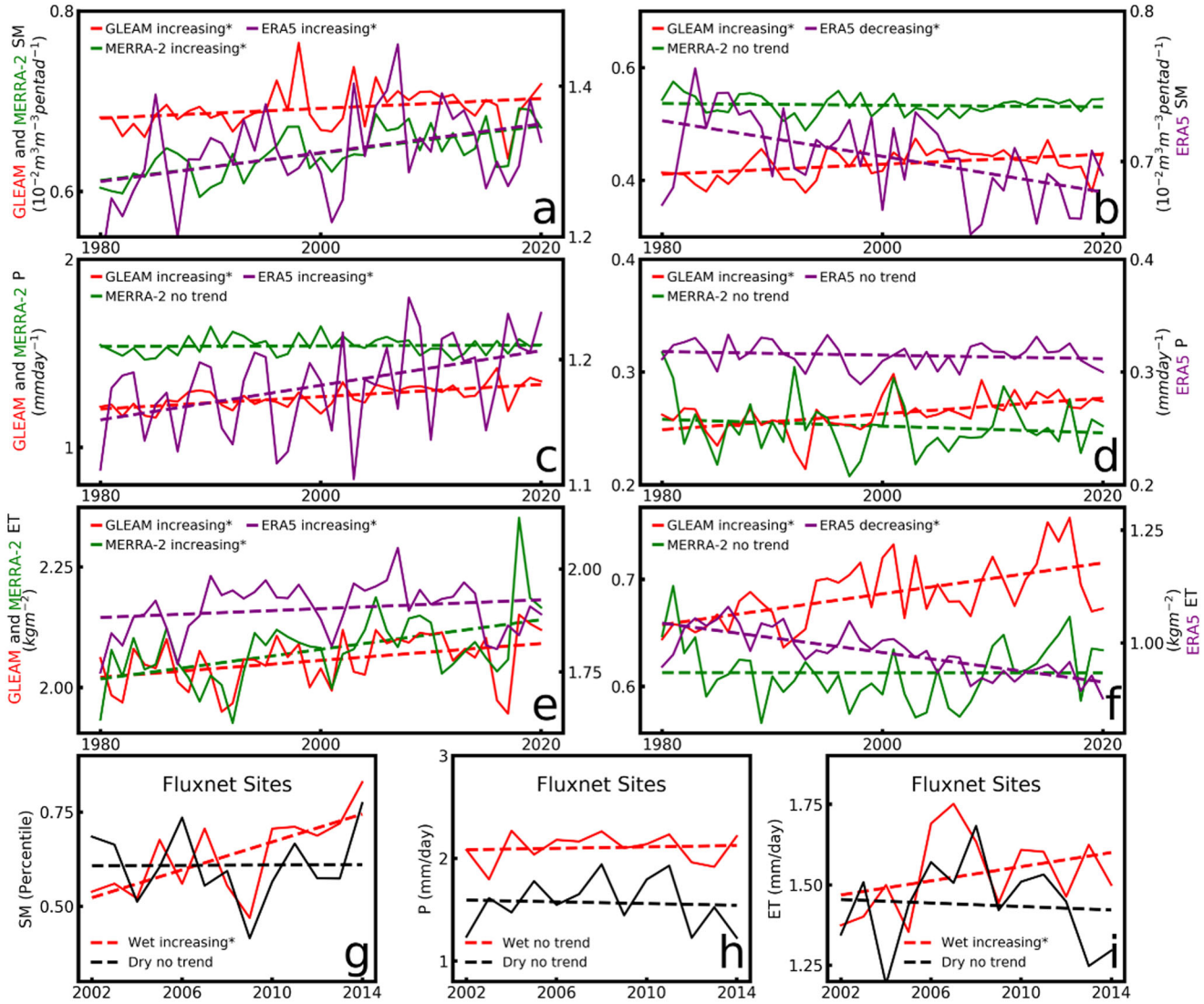

Fig. 2 Trends of annual soil drying rate (in the SM range of 0−30th percentile) and corresponding atmospheric factors in wet and dry regions during 1980–2020 based on ERA5, GLEAM, MERRA-2, and in-situ observation data. a, **b** Trends of annual soil drying rate in wet and dry regions during 1980–2020. **c**, **d** Same as **a**, **b** but for P. **e**, **f** Same as **a**, **b** but for ET. **g**–**i** Trends of annual soil drying rate, P, and ET in wet and dry regions based on in-situ observation data. The linear annual trends of soil drying rate, P, and ET are estimated based on the Sen's slope estimator, and statistical significances in trends are determined based on the MK test. * represents the statistically significant trend at the level of 0.05.

1980–2020 only in wet regions, whereas a consistent increasing trend is not shown in P (Fig. 2c–f). The trends in soil drying rate and ET in wet regions align with those calculated from 80 FLUXNET sites with continuous records (>5 years), despite the fact that these sites' distributions do not represent the entire globe (Supplementary table 1). Similar increasing trends for soil dying rate and corresponding ET and P in wet regions can also be detected when changing the soil drying range from the SM range of 0−30th percentile to 0−25th percentile (Supplementary Fig. 3) and 0−20th percentile (Supplementary Fig. 4). These results indicate that rapid soil drying is in wet regions and accompanied by a significant increase in the mean ET over the past four decades.

Sensitivity of soil drying rate to potential influencing factors

Increased evaporative demand and a critical lack of P are the two main drivers of soil drying. When a P deficit occurs over an extended period of time (e.g., several weeks), SM is depleted by evapotranspiration, yielding increased evaporative stress and the potential for desiccation of the terrestrial surface. Additionally, persistent atmospheric anomalies can increase evaporative demand at the land surface, thereby increasing the evaporative demand and evaporative stress. Thus, we use linear and exponential regressions to analyze the optimal association between the annual soil drying rate and potential atmospheric drivers (i.e., P and ET demand factors: T, VPD, and Rn). A linear regression is identified as the optimal model for T, VPD, and Rn in wet regions, which explains 85%, 63%, and 85% of the interannual variability in the rate of soil drying (Fig. 3a, c, b). However, the fits are insignificant for T, VPD, or Rn in dry regions (Fig. 3e, g, f). Expectedly, the annual soil drying rate is weakly correlated with P, both in wet (4%) and dry (0%) regions (Fig. 3d, h). Indeed, precipitation does not control the drying rate (regulated by evaporative demand), but rather the mean soil moisture state. We also detrend the factors influencing the rate of soil drying using linear regressions, which helps to avoid spurious correlations arising from a common trend. We then estimate the correlation with the annual soil drying rate. The detrended correlations also

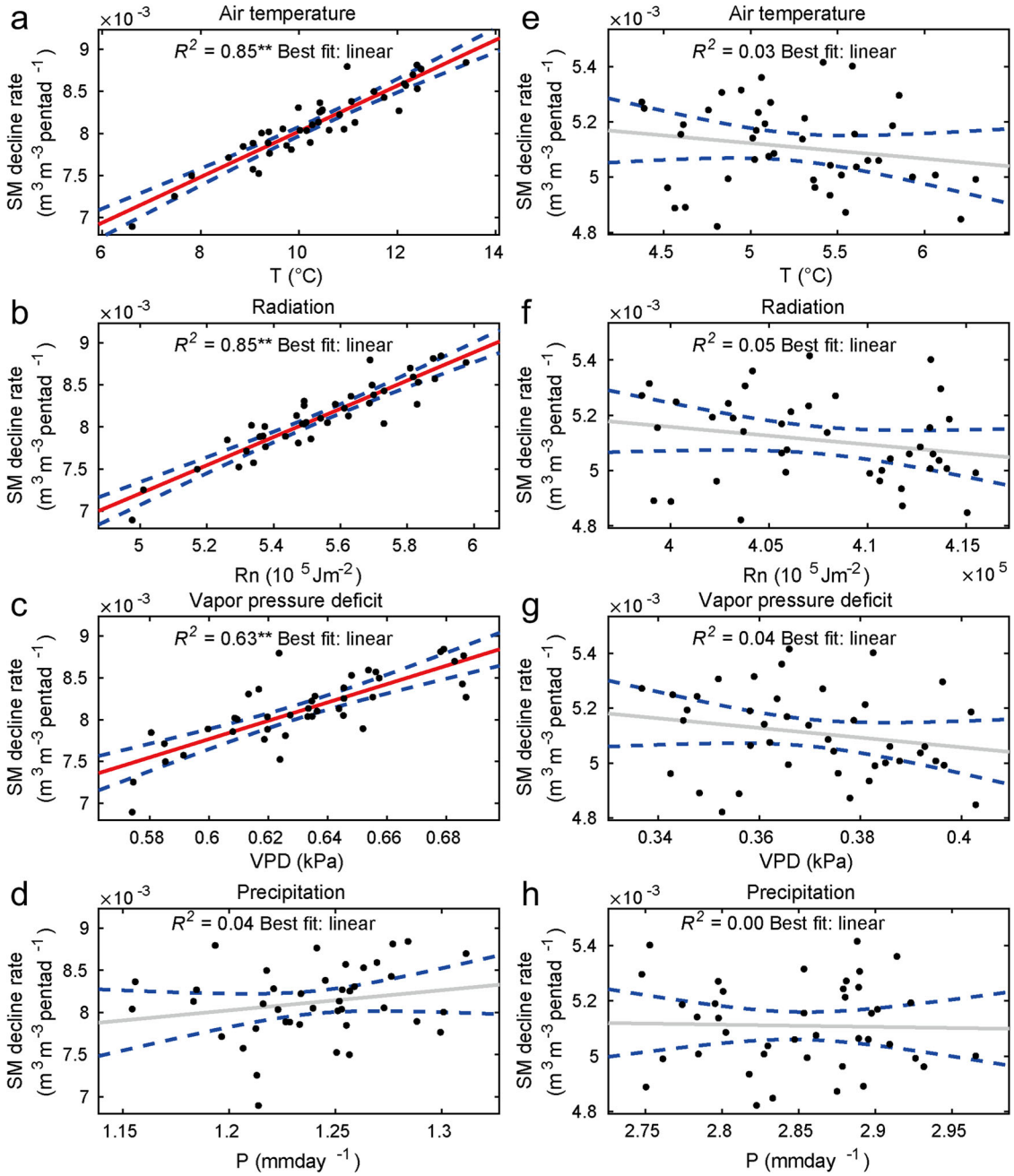

Fig. 3 Regression between the annual soil drying rate and atmospheric factors in wet and dry regions during 1980–2020. a, **e** Regression between the annual soil drying rate and T for wet and dry regions. **b**, **f** Regression between the annual soil drying rate and Rn for wet and dry regions. **c**, **g** Regression between the annual soil drying rate and VPD for wet and dry regions. **d**, **h** Regression between the annual soil drying rate and P for wet and dry regions. Solid lines are the best fit lines derived based on the coefficient of determination (R^2; *$p < 0.05$; **$p < 0.01$). The best fit lines show linear relationships for all the factors. Red solid lines represent a fit with a significant correlation ($p < 0.01$). The dashed lines are the 95% prediction intervals. All results are obtained based on the ensemble mean of ERA5, MERRA-2, and GLEAM.

confirm the relatively high R^2 for T (61%), VPD (39%), and Rn (62%), but the low R^2 for P (Supplementary Fig. 5). Consistent results from linear and exponential regression analyses are obtained for all three datasets (Supplementary Figs. 6−11).

Admittedly, the ET rate is mainly controlled by T, VPD, and Rn, which is also confirmed by linear regressions between these factors and ET (Supplementary Figs. 12−14). Additionally, the significant ($p < 0.01$) causal effects of individual atmospheric factors (i.e., T, VPD, and Rn), except for P, on SM changes are obtained using the convergent cross-mapping technique (see Methods), which can account for the existing causal relationship between these factors and the annual soil drying rate (Fig. 4a–d). And all three datasets confirm similar causal relationships (Supplementary Fig. 15). Compared with the P deficit, therefore, ET changes largely reflect the evaporative demand changes in wet regions and the drying rate is mostly regulated by evaporative demand due to atmospheric aridity and high air temperatures in wet regions. By contrast, there is no consistent causal relationship between atmospheric factors and the annual soil drying rate for three datasets (Supplementary Fig. 16). In dry regions, reduced soil moisture regulates the rate of ET and can compensate for the increased evaporative demand.

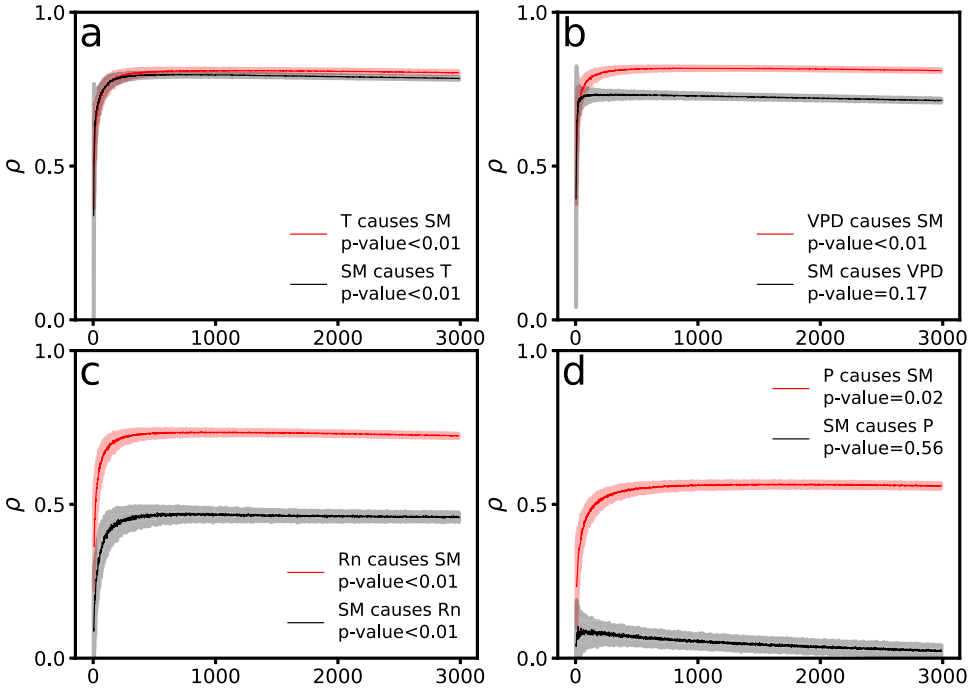

Fig. 4 Detection of causality using convergent cross mapping. a–d Causal relationships of SM − T, SM − VPD, SM−Rn, and SM − P for wet regions using the convergent cross mapping (CCM) for 1980 − 2020. The *x* axis represents the length of time series. The shaded areas show the mean ± SD from bootstrapped iterations. All results are obtained based on the ensemble mean of ERA5, MERRA-2, and GLEAM.

Contribution of interactions between atmospheric factors to rapid soil drying

The interactions between T, VPD, Rn, and P are complex and not fully understood. For example, high T can increase VPD, which in turn can exacerbate water stress and lead to more severe dryness. Similarly, low P combined with high T can lead to more rapid evaporation and SM depletion, increasing the severity of dryness. It is thus essential to study the interactions between T, VPD, Rn, and P to better understand the rate of rapid soil drying.

In addition to the individual causal effects of atmospheric factors (i.e., T, VPD, Rn, and P) on SM changes, we also investigate their combined impacts, including T&VPD, T&Rn, Rn&VPD, T&P, VPD&P, and T&VPD&Rn, on SM changes by multivariate probability distributions (see "Methods" section). We find that SM is significantly ($p < 0.01$) forced by the joint atmospheric variables. Moreover, the causal effects of joint atmospheric variables on SM changes are stronger than those of individual atmospheric factors (Fig. 5). For example, SM is strongly forced by the combination of T and VPD (Pearson correlation coefficient (ρ) = 0.89) (Fig. 5a), whereas SM is relatively weakly forced by T ($\rho = 0.79$) and VPD ($\rho = 0.80$) alone, respectively (Fig. 4a, b). For all possible combinations of factors (i.e., T, VPD, and Rn) associated with ET, the causal effect of T&VPD on SM change is strongest (Fig. 5a–c). Additionally, even though there are relatively weak ($\rho = 0.54$) causal effects of P on SM changes, the causal effects on SM changes become stronger when P is combined with T&VPD, with a higher correlation coefficient between T&VPD&P and SM ($\rho = 0.81$; Fig. 5d). For dry regions, however, the joint causal effects of combined atmospheric factors on SM changes decrease in comparison with individual factors (Supplementary Fig. 17). Compared with individual atmospheric factors, therefore, multiple factors that occur in combination contribute more to the changes in SM in wet regions, which is also confirmed by similar causal relationships for all three datasets (Supplementary Figs. 18−20).

In view of the significant causality of combined atmospheric factors on SM changes, we compare the mean soil drying rates under individual and combined atmospheric factors to confirm the contribution of combined factors on rapid soil drying. Generally, we find that the higher soil drying rates are mostly identified in wet regions (Fig. 5e) and always correspond to larger positive T, VPD, and Rn anomalies as well as negative P anomalies (Supplementary Fig. 21). Specifically, we compare the soil drying rates in which extreme atmospheric factor anomalies occur during soil drying. We find that the regions with combined factor anomalies witness a higher soil drying rate and ET (T&VPD (7.46 $10^{-3}m^3m^{-3}$pentad^{-1}), compared to that with an individual factor anomaly (i.e., T, VPD, Rn, and P) in wet regions (Fig. 5f, g). Such a pattern cannot be obtained in dry regions. The joint effect of T and VPD on the soil drying rate is largely attributed to the land −atmosphere interaction. The close association between soil dryness and combined atmospheric drying and heating tends to exacerbate the intensifying SM decline, resulting in a relatively high decline rate of SM under the mutual amplification of soil dryness and combined atmospheric drying and heating (Supplementary Fig. 22). In dry regions, evapotranspiration may decline during soil drying due to limited soil moisture supply, resulting in reduced bare-soil evaporation and transpiration due to stomatal closure[39]. In this case, further precipitation deficits can be a significant driver of soil drying, and the influence of evapotranspiration on soil drying may vary based on the total water storage anomalies.

Although P is not a strong explanatory variable for the increase in annual soil drying rate based on the linear and causality analyses, P deficit is an essential condition in the soil drying process (i.e., not in the rate but in the mean state). Indeed, soil dryness is often caused by an initial P deficit (Supplementary Fig. 23). Under the conditions of P deficit, the enhanced ET rate is the dominant driver of the soil drying rate. When the surface SM becomes insufficient to supply water for evapotranspiration, initiated by a P deficit, water becomes a limiting factor. Under water-limited conditions, a further increase in evaporation can no longer continue[6,40], even when demand (T and VPD) increases. This is why in dry regions the drying rate is not changing

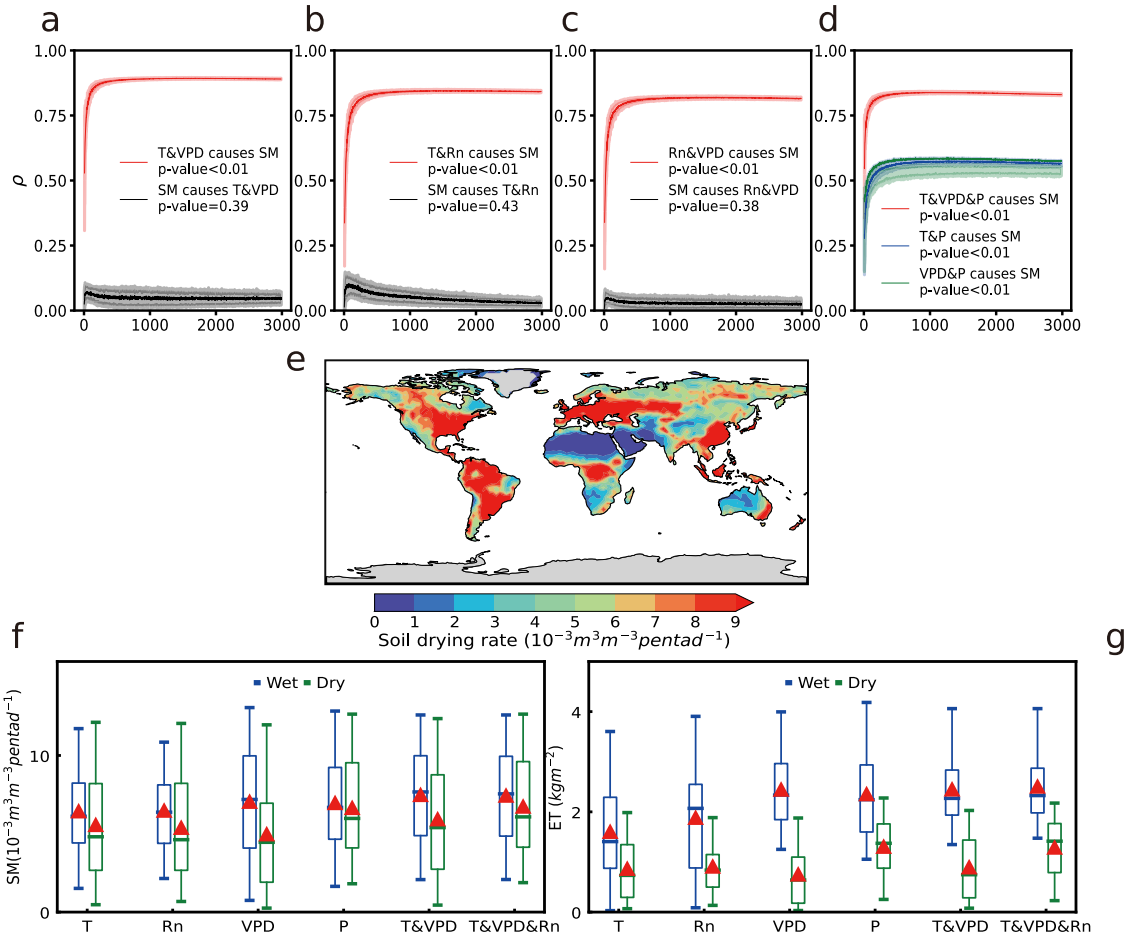

Fig. 5 Influence of interaction between atmospheric factors on soil drying rate. a–d Causal relationships of SM − T&VPD, SM − T&Rn, SM −Rn&VPD, SM − T&P, SM − VPD&P, and SM − T&VPD&P for wet regions using the convergent cross mapping (CCM). The x axis represents the length of time series. The shaded areas show the mean ± SD from bootstrapped iterations. **e** Spatial distribution of mean soil drying rate for 1980 − 2020. **f** Comparison of soil drying rate (mean SM decline rate at the SM ranges of 0−30th percentile) with T anomaly (>1 SD), VPD anomaly (>1 SD), Rn anomaly (>1 SD), and P anomaly (<−1 SD) in wet and dry regions. **g** Same as **f** but for evapotranspiration (ET). The short horizontal line inside the box represents the 50th percentile, and the top and bottom of the box represent the 75th and 25th percentiles, respectively. The top and bottom of the line represent the 95th and 5th percentiles, respectively. The red triangles represent the mean values. All results are obtained based on the ensemble mean of ERA5, MERRA-2, and GLEAM.

drastically, compared to wet regions where more directly track atmospheric demand changes.

DISCUSSION

Compared with deep SM, SM in shallow soil layers responds faster to meteorological anomalies and interacts more closely with the atmosphere and its evaporative demand[41,42]. The water stored in the root-zone layer is directly available to support plant growth, which is a dominant factor affecting agricultural productivity. Thus, the rapid drying rate in the root-zone SM may cause damage to plants and agricultural production. However, the surface SM experiences a much larger decline rate since the top-layer soil responds more directly to evaporative demand increased by higher T and VPD and is not directly influenced by plant stomata (that can mitigate the impact of atmospheric demand changes) unlike deeper rooting depth SM[43,44].

The investigation of soil drying rate and its underlying mechanisms is still at a preliminary stage. For instance, rapid drying in China is often explained as anomalies of meteorological variables compared to slowly developing dryness[45]. In addition, vegetation greening can significantly increase the frequency of rapid drying, such as those which have been shown in the Great Plains and the western United States during warm seasons through enhanced evapotranspiration[46]. Previous studies have indicated that anthropogenic warming may exacerbate rapid drying conditions in China[47]. The rapid drying that occurred in the southeast United States during September of 2019 was associated with an extreme positive Indian Ocean Dipole (IOD)[48]. It is worth noting that although we focus on the contribution of atmospheric factors on the rapid soil drying rate, there are many other factors affecting the rapid decline in SM. For example, vegetation is a key component influencing rapid soil drying considering its important role in mediating the transpiration[49]. Changes in land use, such as deforestation, urbanization, and agricultural expansion, can significantly alter soil moisture dynamics by altering surface runoff, evapotranspiration, and soil structure, potentially resulting in rapid soil drying[50]. Therefore, exploring mechanisms behind soil drying, especially in wet regions, is challenging but a promising direction for unraveling the mystery of rapid soil drying.

We confirm that the enhanced ET rate by increasing demand (T and VPD) plays a dominant role in rapid soil drying. ET is an important feedback mechanism in the climate system, influencing the exchange of energy and water between the land surface and the atmosphere[51]. Enhanced ET due to increasing demand can amplify the warming effect of greenhouse gases and contribute to

positive feedback loops, exacerbating the impacts of climate change. Understanding the role of ET in the climate system can inform climate change mitigation and adaptation strategies, such as reducing greenhouse gas emissions and developing climate-resilient land use practices. Overall, the detection and understanding of the mechanisms of rapid soil drying have far-reaching implications for ecosystem health, agricultural productivity, and climate change adaptation.

Collectively, our findings confirm that soil drying is accelerating in recent decades, especially in wet regions. SM plays a critical role in the cycling of carbon in terrestrial ecosystems. The acceleration of soil drying in wet regions can lead to a decrease in soil organic matter content and a reduction in carbon sequestration potential[52,53]. This can have significant implications for global carbon cycle, as wet regions are often considered important carbon sinks. On the other hand, the soil drying phase intensifies over wet regions compared with dry regions. Vegetation in dry regions may acclimate to local conditions by changing its stomata regulation or xylem properties[54]. However, lower adaptability to dryness for vegetation in wet regions may cause more severe damage and even result in mortality due to poor regulation of vegetation when dryness occurs[55,56]. In addition, the confirmed role of individual and combined atmospheric factors in promoting rapid soil drying has important implications for the occurrence of SM droughts, especially for flash droughts. Identifying the drivers of rapid soil drying and associated factors that may speed up the rapid SM decline is crucial to developing plausible risk mitigation strategies based on multi-criteria analysis of potential weather conditions in different geographical contexts.

METHODS

Definition of dryness condition and drying rate

The rate of change in SM refers to the difference between the current and next-pentad SM, and thus the positive difference is the SM decline rate (unit: $m^3m^{-3}pentad^{-1}$). Since we focus on the SM decline rate during the development of dryness conditions (i.e., SM ≤ 30th percentile) to assess the soil drying rate, we define a pentad as a dryness if the SM is less than (or equal to) the 30th percentile during 1980–2020. Thus, soil drying rate refers to the mean SM decline rate in the range of 0−30th percentile in particular, and the SM decline rate refers to the mean SM decline rate in the whole range of 0−100th percentile. It should be noted that all SM decline is evaluated without requirement regarding the rate of soil moisture decline, and rapidly evolving droughts (i.e., flash droughts) may represent an extreme manifestation within the context of the soil drying we are examining. To avoid the effect of different dryness thresholds on the results, we also choose the 0−25th and 0−20th percentiles to represent the development of dryness conditions to investigate the soil drying rate and corresponding atmospheric anomalies.

Detection of temporal trend

The Mann–Kendall (M-K)[57,58] method is a nonparametric test, which is commonly used for trend detection that examines whether there is a monotonic trend in the time series of the variable of interest. In the M-K test, the null hypothesis, H_0, is that there is no monotonic trend in the series. The alternative hypothesis, H_1, is that the data has a monotonic trend (positive or negative). Positive values of standardized test statistic Z_{MK} indicate an increasing trend in the SM decline rate, whereas negative Z_{MK} values suggest a decreasing trend. The advantages of the M-K test are that statistical analysis is not needed and samples are not required to follow a particular distribution. Thus, this method is not affected by abnormal values, and can be used to well characterize the trend of a time series. The M-K trend analysis was performed in this study to examine the trend of the soil drying rate on a global scale. For a given time series $(x_1, \ldots, x_n)$, the test statistic Z_{MK} was calculated as follows:

$$S = \sum_{i=1}^{n-1} \sum_{j=i+1}^{n} sign(x_j - x_i) \tag{1}$$

$$sign(x_j - x_I) = \begin{cases} +1, & x_j > x_i \\ 0, & x_j = x_i \\ -1, & x_j < x_i \end{cases} \tag{2}$$

$$Var(S) = \frac{1}{18}[n(n-1)(2n+5) - \sum_p t_p(t_p-1)(2t_p+5)] \tag{3}$$

$$Z_{MK} = \begin{cases} \frac{S-1}{\sqrt{Var(S)}} & if\ S > 0 \\ 0 & if\ S = 0 \\ \frac{S+1}{\sqrt{Var(S)}} & if\ S < 0 \end{cases} \tag{4}$$

where n is the length of the time series. x_i and x_j are the sequential data in time series. t_p is the number of ties of the p_{th} value.

Linear regression and exponential regression

We investigate the relationship between atmospheric drivers (independent variable) and the annual soil drying rate (dependent variable) using a linear regression and an exponential regression. The exponential fitting can be described by $y = a^{bx}$, where y and x are the dependent and independent variables, respectively. a and b are the fitting parameters. We evaluate the goodness-of-fit using the R^2 and the p value associated to the correlation. We also investigate the association between the detrended time series of atmospheric drivers and the annual soil drying rate to avoid spurious correlations.

Bivariate copulas

Bivariate copulas are mathematical functions that can be used to describe the dependence between two random variables and to derive their joint distribution. The advantages of copulas are their ability to overcome the shortcoming of assessing the co-occurrence rate of two climate extremes with few samples and the flexibility of capturing the complex dependence between climate variables regardless of their marginal distributions[59]. The joint distribution of random variables X and Y can be expressed as:

$$F_{X,Y}(x,y) = P(X \le x, Y \le y) \tag{5}$$

where X and Y are random variables, and P is their joint distribution. $F_X(x) = P(X \le x)$ and $F_Y(y) = P(Y \le y)$ are the marginal probability distributions of X and Y, respectively. The joint cumulative distribution function (CDF) of X and Y can be expressed as:

$$F_{X,Y}(x,y) = C[F_X(x), F_Y(y)] = C(u,v), 0 \le u,v \le 1 \tag{6}$$

where $F_X(x)$ and $F_Y(y)$ are transformed into two uniformly distributed random variables u and v, and C is a copula function. The copula families, including Gaussian, Student's t, Clayton, Gumbel, and Frank copula, were used to model the dependence structures of random variables. For each grid point, the optimal copula model was selected based on the Bayesian Information Criterion to well represent the dependence structure between two random variables.

The concepts of return level and return period provide critical information for risk assessment and decision-making[60]. The return level with a T-year return period represents an event that has a $1/T$

chance of occurrence in any given year[61]. And the multivariate return period (*RP*) in terms of *X* and *Y* is defined as follows:

$$RP = \frac{\mu}{1 - F_{X,Y}(x,y)} \tag{7}$$

where $\mu > 0$ is the average interarrival time of *X* and *Y* ($\mu = 1/73$ indicates that the average interarrival time between adjacent samples in the time series is 1/73 year).

Here, we use bivariate copulas to characterize the joint probabilities of T&VPD, VPD&P, and T&P and their return periods.

Vine copulas

The bivariate copulas are not flexible in a dimension of three or higher and thus may not well represent the complex interactions of hydroclimate variables in a dimension of three or higher[62,63]. Therefore, vine copulas, a more flexible approach than copulas, are used to construct a joint multivariate probability distribution of T, VPD, and Rn, improving the estimation of the joint return period of T, VPD, and Rn[64]. Assume that *x*, *y*, and *z* signify T, VPD, and Rn, respectively. The joint density $p(x, y, z)$ can be decomposed using vine copulas as follows:

$$\begin{aligned} p(x,y,z) = p(x)\cdot p(y)\cdot p(z)\cdot\ & c(u_x,u_y,\theta_{x,y})\cdot c(u_x,u_z,\theta_{x,z})\cdot \\ & c(h(u_y,u_x,\theta_{x,y}),h(u_z,u_x,\theta_{x,z}),\theta_{y,z|x}) \end{aligned} \tag{8}$$

where $p(x)$, $p(y)$, and $p(z)$ represent the marginal probability density functions (PDFs); *u* represents the marginal cumulative probability; *c* represents the bivariate copula density; $\theta_{x,y}$, $\theta_{x,z}$, and $\theta_{y,z|x}$ represent the parameters of bivariate copulas; the *h*-function is the conditional distribution function. For example, $h(u_y, u_x, \theta_{x,y})$ can be expressed as:

$$h(u_y,u_x,\theta_{x,y}) = F(u_y|u_x) = \frac{\partial C_{x,y}\{F(y),F(x),\theta_{x,y}\}}{\partial F(x)} \tag{9}$$

where $F(x) = u_x$ and $F(y) = u_y$ represent the marginal CDFs. Since the vine structure (i.e., Eq. (8)) varies with the order of variables and the bivariate copula families, the sequential maximal spanning tree algorithm and the BIC are used to identify an appropriate structure[65]. After determining the vine structure, the joint cumulative probability of T, VPD, and Rn, $F_{X,Y,Z}(x, y, z)$, can be estimated through a three-dimensional numerical integration for Eq. (8). Such estimates are inserted into Eq. (10) to calculate the joint return periods of T, VPD, and Rn.

$$RP(x,y,z) = \frac{\mu}{1 - F_{X,Y,Z}(x,y,z)} \tag{10}$$

where $\mu > 0$ is the average interarrival time of *X*, *Y*, and *Z* ($\mu = 1/73$ indicates that the average interarrival time between adjacent samples in the time series is 1/73 year).

Detection of causal relationships: convergent cross mapping

The bivariate copula and vine copula approaches provide joint variables, namely the return period of T&VPD, T&P, VPD&P, and T&VPD&P, that integrate the temporal information of concurrent atmospheric factors. Such joint return periods are used as the causal variable *X* to examine the causal relationships between concurrent atmospheric factors and SM based on Convergent cross mapping (CCM).

CCM is a powerful approach that can help distinguish causality from spurious correlation in time series of non-linear dynamical systems[66,67]. In CCM, causality is detected by measuring the extent to which the historical record of the affected variable *Y* (or its proxies) reliably estimates the states of a causal variable *X*. That is, if variable *X* is influencing *Y*, then, based on the generalized Takens' theorem, the causal variable *X* can be recovered from the historical record of the affected variable *Y*. The skill of cross mapping is defined as the coefficient ρ of correlation between predictions and observations of *X*. If the ρ increases with the length of the time series and convergence is present, then the causal effect of *X* on *Y* can be inferred. A simple model system consisting of 2 coupled logistic differentia equations can be expressed as

$$X(t+1) = X(t)(r_x - r_x X(t) - \beta_{x,y} Y(t)) \tag{11}$$

$$Y(t+1) = Y(t)(r_y - r_y Y(t) - \alpha_{y,x} X(t)) \tag{12}$$

where *t* and $t+1$ are the time steps. r_x and r_y are the variables' intrinsic growth rates, and $\beta_{x,y}$ and $\alpha_{y,x}$ represent the impacts of variable *X* on the dynamics of variable *Y* and the impacts of variable *Y* on the dynamics of variable *X*, respectively.

In this study, the CCM analysis was implemented using the multispatial CCM package in the R language environment. We analyze the dynamical systems using optimal embedding dimension estimated by simplex projection, and $\tau = 1$ (time lags), iteration = 1000 (the number of bootstrap iterations) based on the pentad data for the study period.

Definition of dryland

The global wet and dry regimes (Supplementary Fig. 24) can be identified as the regions with an aridity index (AI). The aridity index (AI), expressed as the ratio of potential evaporation (Ep) to precipitation (P), is a widely used indicator of regional moisture conditions. The interplay between water supply and demand, including both Ep and P, is critical to the assessment of changes in dryness and dryland dynamics. The AI can thus be calculated based on the ratio between average annual Ep and P using monthly Ep and P from the Climatic Research Unit (CRU), which represents the characteristics of dryness/desertification over a specific region.

$$AI = \frac{Ep}{P}\begin{cases} Dry & (AI > 1.5) \\ Wet & (AI \le 1.5) \end{cases} \tag{13}$$

DATA AVAILABILITY

SM data

Daily surface SM were obtained from the European Centre for Medium-Range Weather Forecasts (ERA5) (https://www.ecmwf.int/en/forecasts/datasets/reanalysis-datasets/era5), the Modern-Era Retrospective Analysis for Research and Applications, version 2 (MERRA-2) (https://disc.gsfc.nasa.gov), and the Global Land Evaporation Amsterdam Model (GLEAM) (https://www.gleam.eu/) datasets. The ERA5, MERRA-2, and GLEAM SM datasets are observationally constrained, which have been widely used to analyze global and regional SM changes. The daily SM data from three datasets were aggregated to the same resolution of 2.5° × 2.5° and a temporal resolution of pentads for 1980−2020. Finally, we aggregate the daily values to pentad averages.

FLUXNET2015

To compare the soil drying trend with ground-level observations, we selected 80 sites in the FLUXNET2015 datasets across the globe (Supplementary table 1). Sites were chosen to ensure that SM, P, and latent heat fluxes were collected for more than 5 years.

Climatic data

We use daily climatic data from the ERA5 and MERRA-2 to calculate daily VPD. Daily VPD was calculated as the difference between saturated water vapor pressure, determined by near-surface T, and actual water vapor pressure, determined by the dew-point T. In addition to T and VPD, Rn and P were also obtained from the ERA5 and MERRA-2. As for the GLEAM, daily P from the Multi-Source Weighted Ensemble Precipitation (MSWEP) (http://www.gloh2o.org/mswep/), together with near-surface T, Rn, and VPD from ERA5, were used to assess the relationship between GLEAM SM and atmospheric factors. ET was calculated from latent heat flux in ERA5 and MERRA-2, and ET is represented by actual evaporation in GLEAM. In addition, the monthly Ep and P from the Climatic Research Unit (CRU) (https://crudata.uea.ac.uk/cru/data/hrg/) were used to calculate AI for classifying arid/humid zones across the globe. All these data were aggregated to the same resolution of SM data and a temporal resolution of pentads for 1980 − 2020.

CODE AVAILABILITY

The codes used in this study are available from the corresponding author upon reasonable request.

Received: 9 August 2023; Accepted: 22 November 2023;
Published online: 08 December 2023

REFERENCES

1. D'Odorico, P. & Porporato, A. Preferential states in soil moisture and climate dynamics. *Proc. Natl Acad. Sci. USA* **101**, 8848–8851 (2004).
2. Huntington, T. G. Evidence for intensification of the global water cycle: review and synthesis. *J. Hydrol.* **319**, 83–95 (2006).
3. Zhou, S. et al. Soil moisture–atmosphere feedbacks mitigate declining water availability in drylands. *Nat. Clim. Change* **11**, 38–44 (2021).
4. Bastiaanssen, W. G. SEBAL-based sensible and latent heat fluxes in the irrigated Gediz Basin, Turkey. *J. Hydrol.* **229**, 87–100 (2000).
5. Teuling, A. J. & Seneviratne, S. I. Contrasting spectral changes limit albedo impact on land-atmosphere coupling during the 2003 European heat wave. *Geophys. Res. Lett.* **35**, L03401 (2008).
6. Seneviratne, S. I. et al. Investigating soil moisture–climate interactions in a changing climate: a review. *Earth Sci. Rev.* **99**, 125–161 (2010).
7. Falloon, P., Jones, C. D., Ades, M. & Paul, K. Direct soil moisture controls of future global soil carbon changes: an important source of uncertainty. *Glob. Biogeochem. Cycles* **25**, 6495–6503 (2011).
8. Trugman, A. T., Medvigy, D., Mankin, J. S. & Anderegg, W. R. Soil moisture stress as a major driver of carbon cycle uncertainty. *Geophys. Res. Lett.* **45**, 6495–6503 (2018).
9. Green, J. K. et al. Large influence of soil moisture on long-term terrestrial carbon uptake. *Nature* **565**, 476–479 (2019).
10. Humphrey, V. et al. Soil moisture–atmosphere feedback dominates land carbon uptake variability. *Nature* **592**, 65–69 (2021).
11. Liu, N. et al. Improvement of a simplified process-based model for estimating transpiration under water-limited conditions. *Hydrol. Process.* **33**, 1670–1685 (2019).
12. Song, X., Lyu, S. & Wen, X. Limitation of soil moisture on the response of transpiration to vapor pressure deficit in a subtropical coniferous plantation subjected to seasonal drought. *J. Hydrol.* **591**, 125301 (2020).
13. Liu, L. et al. Soil moisture dominates dryness stress on ecosystem production globally. *Nat. Commun.* **11**, 1–9 (2020).
14. Yan, N., Marschner, P., Cao, W., Zuo, C. & Qin, W. Influence of salinity and water content on soil microorganisms. *Int. Soil Water Conserv. Res.* **3**, 316–323 (2015).
15. Borowik, A. & Wyszkowska, J. Soil moisture as a factor affecting the microbiological and biochemical activity of soil. *Plant Soil Environ.* **62**, 250–255 (2016).
16. Moreno-Espíndola, I. P. et al. The bacterial community structure and microbial activity in a traditional organic milpa farming system under different soil moisture conditions. *Front. Microbiol.* **9**, 2737 (2018).
17. Brolsma, R. J. & Bierkens, M. F. P. Groundwater–soil water–vegetation dynamics in a temperate forest ecosystem along a slope. *Water Resour. Res.* **43**, W01414 (2007).
18. D'Odorico, P., Caylor, K., Okin, G. S. & Scanlon, T. M. On soil moisture–vegetation feedbacks and their possible effects on the dynamics of dryland ecosystems. *J. Geophys. Res. Biogeosci.* **112**, G4 (2007).
19. Sawada, Y., Koike, T. & Walker, J. P. A land data assimilation system for simultaneous simulation of soil moisture and vegetation dynamics. *J. Geophys. Res. Atmos.* **120**, 5910–5930 (2015).
20. Dorigo, W. et al. Evaluating global trends (1988–2010) in harmonized multi-satellite surface soil moisture. *Geophys. Res. Lett.* **39**, 18 (2012).
21. Cheng, S. & Huang, J. Enhanced soil moisture drying in transitional regions under a warming climate. *J. Geophys. Res. Atmos.* **121**, 2542–2555 (2016).
22. Schwalm, C. R. et al. Global patterns of drought recovery. *Nature* **548**, 202–205 (2017).
23. Berg, A. & Sheffield, J. Climate change and drought: the soil moisture perspective. *Curr. Clim. Change Rep.* **4**, 180–191 (2018).
24. Kozlowski, T. T. & Pallardy, S. G. Acclimation and adaptive responses of woody plants to environmental stresses. *Bot. Rev.* **68**, 270–334 (2002).
25. Flexas, J., Bota, J., Galmés, J., Medrano, H. & Ribas-Carbó, M. Keeping a positive carbon balance under adverse conditions: responses of photosynthesis and respiration to water stress. *Physiol. Plant.* **127**, 343–352 (2006).
26. Jones, H. G. Monitoring plant and soil water status: established and novel methods revisited and their relevance to studies of drought tolerance. *J. Exp. Bot.* **58**, 119–130 (2007).
27. Kim, J. & van Iersel, M. W. Slowly developing drought stress increases photosynthetic acclimation of Catharanthus roseus. *Physiol. Plant.* **143**, 166–177 (2011).
28. Chaves, M. M., Maroco, J. P. & Pereira, J. S. Understanding plant responses to drought—from genes to the whole plant. *Funct. Plant Biol.* **30**, 239–264 (2003).
29. Mukherjee, S., Mishra, A. K., Zscheischler, J. & Entekhabi, D. Interaction between dry and hot extremes at a global scale using a cascade modeling framework. *Nat. Commun.* **14**, 277 (2023).
30. Ambika, A. K. & Mishra, V. Modulation of compound extremes of low soil moisture and high vapor pressure deficit by irrigation in India. *J. Geophys. Res. Atmos.* **126**, e2021JD034529 (2021).
31. Christian, J. I., Basara, J. B., Hunt, E. D., Otkin, J. A. & Xiao, X. Flash drought development and cascading impacts associated with the 2010 Russian heatwave. *Environ. Res. Lett.* **15**, 094078 (2020).
32. Stocker, B. D. et al. Drought impacts on terrestrial primary production underestimated by satellite monitoring. *Nat. Geosci.* **12**, 264–270 (2019).
33. Nguyen, H. et al. Using the evaporative stress index to monitor flash drought in Australia. *Environ. Res. Lett.* **14**, 064016 (2019).
34. Pendergrass, A. G. et al. Flash droughts present a new challenge for subseasonal-to-seasonal prediction. *Nat. Clim. Change* **10**, 191–199 (2020).
35. Qing, Y., Wang, S., Ancell, B. C. & Yang, Z. L. Accelerating flash droughts induced by the joint influence of soil moisture depletion and atmospheric aridity. *Nat. Commun.* **13**, 1–10 (2022).
36. Zhou, S. et al. Land–atmosphere feedbacks exacerbate concurrent soil drought and atmospheric aridity. *Proc. Natl Acad. Sci. USA* **116**, 18848–18853 (2019).
37. Lawlor, D. W. & Cornic, G. Photosynthetic carbon assimilation and associated metabolism in relation to water deficits in higher plants. *Plant Cell Environ.* **25**, 275–294 (2002).
38. López, R., Rodríguez-Calcerrada, J. & Gil, L. Physiological and morphological response to water deficit in seedlings of five provenances of Pinus canariensis: potential to detect variation in drought-tolerance. *Trees* **23**, 509–519 (2009).
39. Gupta, A., Rico-Medina, A. & Caño-Delgado, A. I. The physiology of plant responses to drought. *Science* **368**, 266–269 (2020).
40. Gentine, P., Chhang, A., Rigden, A. & Salvucci, G. Evaporation estimates using weather station data and boundary layer theory. *J. Geophys. Res.* **43**, 11–661 (2016).
41. Wang, Y. et al. Grassland soil moisture fluctuation and its relationship with evapotranspiration. *Ecol. Indic.* **131**, 108196 (2021).
42. Li, X. & Huang, W. R. How long should the pre-existing climatic water balance be considered when capturing short-term wetness and dryness over China by using SPEI? *Sci. Total Environ.* **786**, 147575 (2021).
43. Jafari, M., Kamali, H., Keshavarz, A. & Momeni, A. Estimation of evapotranspiration and crop coefficient of drip-irrigated orange trees under a semi-arid climate. *Agric. Water Manag.* **248**, 106769 (2021).
44. Potkay, A. et al. Coupled whole-tree optimality and xylem hydraulics explain dynamic biomass partitioning. *New Phytol.* **230**, 2226–2245 (2021).
45. Yuan, X. et al. Anthropogenic shift towards higher risk of flash drought over China. *Nat. Commun.* **10**, 1–8 (2019).
46. Chen, L., Ford, T. W. & Yadav, P. The role of vegetation in flash drought occurrence: a sensitivity study using Community Earth System Model, Version 2. *J. Hydrometeorol.* **22**, 845–857 (2021).
47. Wang, L., Yuan, X., Xie, Z., Wu, P. & Li, Y. Increasing flash droughts over China during the recent global warming hiatus. *Sci. Rep.* **6**, 1–8 (2016).
48. Schubert, S. D., Chang, Y., DeAngelis, A. M., Wang, H. & Koster, R. D. On the development and demise of the Fall 2019 Southeast US flash drought: Links to an extreme positive IOD. *J. Clim.* **34**, 1701–1723 (2021).
49. Yang, R. & Friedl, M. A. Modeling the effects of three-dimensional vegetation structure on surface radiation and energy balance in boreal forests. *J. Geophys. Res. Atmos.* **108**, D16 (2003).
50. Wang-Erlandsson, L. et al. A planetary boundary for green water. *Nat. Rev. Earth Environ.* **3**, 380–392 (2022).
51. Trenberth, K. E. & Shea, D. J. Relationships between precipitation and surface temperature. *Geophys. Res. Lett.* **32**, 14 (2005).
52. Manzoni, S., Schimel, J. P. & Porporato, A. Responses of soil microbial communities to water stress: results from a meta-analysis. *Ecology* **93**, 930–938 (2012).
53. Davidson, E. A. & Janssens, I. A. Temperature sensitivity of soil carbon decomposition and feedbacks to climate change. *Nature* **440**, 165–173 (2006).
54. Xue, B. et al. Global convergence but regional disparity in the hydrological resilience of ecosystems and watersheds to drought. *J. Hydrol.* **591**, 125589 (2020).
55. Li, K., Tong, Z., Liu, X., Zhang, J. & Tong, S. Quantitative assessment and driving force analysis of vegetation drought risk to climate change: Methodology and application in Northeast China. *Agric. Meteorol.* **282**, 107865 (2020).
56. Ma, X., Huete, A., Moran, S., Ponce-Campos, G. & Eamus, D. Abrupt shifts in phenology and vegetation productivity under climate extremes. *J. Geophys. Res. Biogeosci.* **120**, 2036–2052 (2015).

57. Mann, H. B. Nonparametric tests against trend. *Econometrica* **13**, 245–259 (1945).
58. Kendall, M. G. *Rank Correlation Methods*. 4th edn, Vol. 272 (Charles Griffin, 1975).
59. Zscheischler, J. & Seneviratne, S. I. Dependence of drivers affects risks associated with compound events. *Sci. Adv.* **3**, e1700263 (2017).
60. Rosbjerg, D. & Madsen, H. *Design with uncertain design values. In International Conference on Hydrology in a Changing Environment* (pp. 155−163). (Wiley, 1998).
61. Cooley, D., Nychka, D. & Naveau, P. Bayesian spatial modeling of extreme precipitation return levels. *J. Am. Stat. Assoc.* **102**, 824–840 (2007).
62. Zhang, B., Wang, S., Moradkhani, H., Slater, L. & Liu, J. A vine copula-based ensemble projection of precipitation intensity-duration-frequency curves at sub-daily to multi-day time scales. *Water Resour. Res.* **58**, e2022WR032658 (2022).
63. Bevacqua, E., Maraun, D., Hobæk Haff, I., Widmann, M. & Vrac, M. Multivariate statistical modelling of compound events via pair-copula constructions: analysis of floods in Ravenna (Italy). *Hydrol. Earth Syst. Sci.* **21**, 2701–2723 (2017).
64. Zhang, B., Wang, S. & Wang, Y. Probabilistic projections of multidimensional flood risks at a convection-permitting scale. *Water Resour. Res.* **57**, e2020WR028582 (2021).
65. Dißmann, J., Brechmann, E. C., Czado, C. & Kurowicka, D. Selecting and estimating regular vine copulae and application to financial returns. *Comput. Stat. Data Anal.* **59**, 52–69 (2013).
66. Sugihara, G. et al. Detecting causality in complex ecosystems. *Science* **338**, 496–500 (2012).
67. Clark, A. T. et al. Spatial convergent cross mapping to detect causal relationships from short time series. *Ecology* **96**, 1174–1181 (2015).

ACKNOWLEDGEMENTS

The work described in this paper was partially supported by a grant from the Research Grants Council of the Hong Kong Special Administrative Region, China (Project No. PolyU/RGC 15232023) and the Hong Kong Polytechnic University (Project No. P0045957, P0043040).

AUTHOR CONTRIBUTIONS

S.W. conceived and supervised the study. Y.Q. and S.W. carried out the analysis and wrote the paper. Y.Q. and S.W. contributed equally to this work. Z.L.Y and P.G. provided comments and suggestions for improving the quality of this paper. B.Z. and J.A. edited the manuscript.

COMPETING INTERESTS

The authors declare no competing interests.

ADDITIONAL INFORMATION

Supplementary information The online version contains supplementary material available at https://doi.org/10.1038/s41612-023-00531-y.

Correspondence and requests for materials should be addressed to Shuo Wang.

Reprints and permission information is available at http://www.nature.com/reprints

Publisher's note Springer Nature remains neutral with regard to jurisdictional claims in published maps and institutional affiliations.

Open Access This article is licensed under a Creative Commons Attribution 4.0 International License, which permits use, sharing, adaptation, distribution and reproduction in any medium or format, as long as you give appropriate credit to the original author(s) and the source, provide a link to the Creative Commons license, and indicate if changes were made. The images or other third party material in this article are included in the article's Creative Commons license, unless indicated otherwise in a credit line to the material. If material is not included in the article's Creative Commons license and your intended use is not permitted by statutory regulation or exceeds the permitted use, you will need to obtain permission directly from the copyright holder. To view a copy of this license, visit http://creativecommons.org/licenses/by/4.0/.

© The Author(s) 2023